1 (2026) 100017

Contents lists available at ScienceDirect

Chemical Engineering Journal: Green and Sustainable

journal homepage: www.sciencedirect.com/journal/chemical-engineering-journal-green-and-sustainable

Operando and *ex situ* comparison of Pt and Pt_3Co catalyst degradation under ORR in PEMFC

Marco Bogar [a,*], Yurii Yakovlev [b], Simone Pollastri [c,d], Tomáš Hrbek [b], David Kalabis [b], Giovanna Marussi [e], Matteo Crosera [e], Roberto Biagi [c,f,g], Heinz Amenitsch [h], Rodolfo Taccani [a], Iva Matolínová [b]

[a] *Department of Engineering and Architecture, University of Trieste, Via Alfonso Valerio 6/1, 34127 Trieste, Italy*
[b] *Department of Surface and Plasma Science, Faculty of Mathematics and Physics, Charles University, V Holešovičkách 2, 180 00 Prague 8, Czech Republic*
[c] *Department of Physics, Computer Science and Mathematics, University of Modena and Reggio Emilia, 41125 Modena, Italy*
[d] *ELETTRA - Sincrotrone Trieste S.C.p.A., SS 14 – km 163, 5, 34149, Basovizza, Trieste, Italy*
[e] *Department of Chemical and Pharmaceutical Sciences, University of Trieste, Via Giorgeri 1, Trieste 34127, Italy*
[f] *Istituto Nanoscienze (NANO-S3), Consiglio Nazionale delle Ricerche (CNR), via G. Campi 213/a, Modena 41125, Italy*
[g] *Centro H2-MORE, University of Modena and Reggio Emilia, 41125 Modena, Italy*
[h] *Graz University of Technology, Institute for Inorganic Chemistry, Stremayrgasse 9, 8010 Graz, Austria*

A R T I C L E I N F O

Keywords:
PEMFC performances
Oxygen Reduction Reaction
Bimetallic alloys
Electrochemically Active Surface Area
Operando
Degradation mechanisms

A B S T R A C T

Platinum bimetallic alloys represent a promising class of catalysts for the oxygen reduction reaction in proton exchange membrane fuel cells. Among them, Pt_3Co is characterised by higher performances than bare Pt, but also by different stability, as Co leaching is known to take place during fuel cell operation. To underline differences of catalyst behaviour in real operating conditions, the evolution of bare Pt and Pt_3Co catalyst nanoparticles are here compared from pristine conditions, up to catalyst activation and aging *via* specific break-in and Accelerated Stress Tests (ASTs) procedures, respectively. Changes in catalyst chemistry were monitored *via* x-ray absorption and photoelectron spectroscopies, and *via* SEM-EDX. Results were combined with morphology analysis carried out *via* small-angle x-ray scattering. Results from both *operando* and *ex situ* measurements show as for bare Pt catalyst, both particle morphology and the ratio among metal-to-oxidised Pt do not change remarkably after the break-in, and that the Electrochemically Active Surface Area (ECSA) strongly reduces due to average particle size growth from 2.28 to 6.21 nm within the first 3000 AST cycles. Conversely, in Pt_3Co catalyst, Co leaching strongly affects the break-in stage, by reducing particle size and decreasing the fraction of metallic Co. During ASTs, leaching continues also after the formation of the Pt-rich skin, which formation contributes to slow down ECSA reduction, with particle size growing from 2.59 to 6.14 nm in between 3000 and 6000 cycles only.

1. Introduction

Proton Exchange Membrane Fuel Cells (PEMFCs) constitute the reference technology for hydrogen-fuelled zero-emission power generation. Characterised by satisfying performances in terms of specific power and peak efficiency, PEMFC diffusion on the market is still limited by technology costs and durability directly related to the catalyst layer composition [1]. With the aim of reducing costs, in the last decades platinum catalyst loading has been progressively reduced [2]. In addition, different approaches were successfully adopted to optimize catalyst structure at the nanoscale [3–5] either by designing single-atom catalysts [6], or by alloying platinum with transition metals (Ni, Co, Y, *etc.*) [5] to tune platinum electronic structure and leverage ligand-strain effects, forming for example core–shell nanostructures, or single–atom catalyst materials. Among all of the different alloys investigated, both $Pt_XNi_{(1-X)}$ and $Pt_XCo_{(1-X)}$ demonstrated to be valid alternatives to bare Pt catalyst nanoparticles, showing even better performances with respect to standard Pt-based catalysts, due to the strain effect induced by the alloy formation [7–13].

Nonetheless, the degradation kinetics of platinum bimetallic alloys differ from those of bare Pt catalyst materials [14,15], as the dealloying of the less noble metal was reported to play a crucial role affecting the

* Corresponding author at: Department of Engineering and Architecture, University of Trieste, Via A. Valerio 10/1, 34127 Trieste (TS), Italy.
E-mail address: marco.bogar@dia.units.it (M. Bogar).

https://doi.org/10.1016/j.cejgas.2025.100017
Received 25 September 2025; Received in revised form 12 November 2025; Accepted 8 December 2025
Available online 11 December 2025

performances and stability of the catalyst in both $Pt_XNi_{(1-X)}$ [16–18] and $Pt_XCo_{(1-X)}$ [19,20] formulations. While complex ternary or quaternary alloys are under investigation with the aim of finding stabilization mechanisms able to reduce dealloying, and consequently extend catalyst lifetime over time, in-depth analyses of the effects of metal dealloying are still limited in number. To date, it has been observed that the dissolution of the less noble metal strongly influences catalyst reaction kinetics [8,19], and that the consequent formation of a Pt-rich skin plays an important role in slowing down the catalyst degradation rate [15,21,22].

With the aim of shedding light on catalyst evolution in fuel cells and water electrolysers, in previous works, we presented an electrochemical cell [23] and an experimental approach [24] combining *operando* electrochemical analysis based on x-ray-based investigation techniques to the depict change of chemistry and morphology of catalyst nanoparticles, by means of X-ray Absorption Spectroscopy (XAS) and Small-Angle X-ray Scattering (SAXS), respectively. Obtained results have been complemented by means of SEM-EDX, *operando* XPS and Inductively Coupled Plasma Mass Spectroscopy (ICP-MS). In this work, we aim to highlight the differences in degradation between bare Pt and Pt_3Co catalyst nanoparticles for the Oxygen Reduction Reaction (ORR) in low-temperature PEMFCs, undergoing properly designed Accelerated Stress Tests (ASTs) simulating load cycling conditions. As already done on half-cells [25,26] or full cells [27–29], we aim to better understand degradation dynamics, and provide a benchmark for further studies addressing the development of novel formulations for catalyst materials [30–32]. Furthermore, we show that leaching taking place during the break-in step is fundamental in defining the stability of platinum-bimetallic alloys under subsequent fuel cell operation, as recently demonstrated for Pt—Ni bimetallic alloy too [33].

2. Materials and methods

2.1. MEA preparation

Membrane Electrode Assemblies (MEAs) were made starting from self-made Catalyst Coated Membranes (CCMs), prepared by ultrasonic spraying a catalyst ink on the surface of Nafion (NR-212, Fuel Cell Store) *via* a CNC controlled system (ExactaCoat, Sono-Tek), as detailed in previous works [34,35]. MEAs with a cathode catalyst layer containing Pt catalyst and Pt_3Co, were prepared using catalyst inks with Pt/C (Pt on Vulcan XC-72R, 40 wt%; FuelCellStore) and Pt_3Co/C (Pt_3Co on Vulcan XC-72R, containing 40 wt% of Pt_3Co; FuelCellStore) catalyst nanoparticles, respectively. The catalyst inks were prepared with a ionomer-to-carbon ratio equal to 0.6 [34] by the ultrasonic mixing of the catalyst nanoparticles with ionomer dispersion D521 (5 % 1100 EW; FuelCellStore) and isopropanol/water solvent (1:1 ratio). The ink was sonicated for 15 minutes using a horn-type sonicator (HD-3100, Bandeling SonoPulse). For ultrasonic spraying process the membranes were secured on a hot-bed (60 °C) to ensure rapid evaporation of the solvent. The cathode electrodes of the CCMs measured *via* XAS were loaded with 0.4 $mg{\cdot}cm^{-2}$, while loading was doubled (to 0.8 $mg{\cdot}cm^{-2}$) for SAXS analysis, to guarantee catalyst detectability. Conversely, the anode electrodes were loaded with Pd/C (Pd on Vulcan XC-72R, 40 wt% of Pd; FuelCellStore, loading of 0.2 $mg_{Pd}{\cdot}cm^{-2}$) for XAS measurements to avoid any contamination of the XAS signal recorded in transmission mode from the catalyst layer deposited on the anode side, as previously done [23]. Being SAXS not chemically sensitive, and due to the fast kinetics characterising the hydrogen oxidation reaction, Pt/C catalyst was used with reduced loading (0.05 $mg_{Pt}{\cdot}cm^{-2}$) to avoid detecting the scattering pattern produced by the anodic particle population, as previously done [23]. Finally, two commercial Gas Diffusion Layers (GDLs, H24C5, Freudenberg) were used to sandwich the CCMs.

2.2. X-ray Absorption Spectroscopy (XAS)

XAS spectra were collected at the XAFS beamline [36] of ELETTRA synchrotron, using a fixed exit Si (111) monochromator, at the L_3- and K-edges of Pt and Co, in transmission and fluorescence mode, using respectively ionization chambers and Silicon Drift Detectors (SDD). A KETEK (GmbH AXAS-M, Munich, Germany, active area: 80 mm^2) SDD detector was used during *operando* measurements, whereas for spectra collected *ex situ* a high-performance multichannel SDD detector (AXPiDe v2.0, Agostini et al. 2025) [37] was employed. The beamline uses a collimated x-ray beam, whose size at the exit slits was equal to 0.6 × 0.5 mm^2. Energy calibration was accomplished by collecting simultaneously a spectrum of a metallic reference placed in a second experimental chamber, with the position of the first inflection point settled to 11564 and 7709 eV for Pt and Co, respectively. Spectra of Pt- and Co-bearing reference compounds were either already available from previous experiments conducted at the same beamline [23,38], or provided by the database available at the beamline itself. All of the spectra were collected with an energy step dependant on the energy of the incoming beam: 5 eV steps in the first 200 eV of the spectrum, 0.2 eV step in the XANES region, and a k-constant step of 0.03 $Å^{-1}$ in the EXAFS region. The XANES spectra of the samples and model compounds were normalized to unity by means of Athena software [39]. EXAFS refinements were also conducted on the *ex situ* data of the pristine samples: signals were extracted using the Athena software, Fourier-transformed with a Hanning window in the k range 3 ÷ 11 $Å^{-1}$ and quantitative analyses were carried out using the Artemis software (Demeter 0.9.25 package) [39]. The shell for metallic Pt and the shells for the Pt_3Co alloy have been calculated using the crystallographic data reported by Wyckoff [40] and by Geisler and Martin [41], respectively. XANES data of the samples were analysed also by linear combination fitting approach with the Athena software, by using spectra from the reference compounds, to estimate the average oxidation state.

2.3. Small-Angle X-ray Scattering (SAXS)

Ex situ and *operando* SAXS patterns were collected on the Austrian SAXS beamline at the ELETTRA synchrotron in Trieste, Italy [42], at room temperature and pression, in transmission mode. at a wavelength of 0.77 Å (16 keV), with a beam size of 0.8 × 0.5 mm^2 and a sample-to-detector distance set to 2225.7 mm. Patterns were recorded *via* a 2D pixel detector (Pilatus 3 1 M, Dectris), and radially integrated by means of SAXSDOG [43] software. As calibrant, silver behenate was used. Scattering patterns were analysed within the q-range from 0.097 nm^{-1} to 6.376 nm^{-1} by using IGOR Pro software (IGOR Pro 7.0.8.1, Wavemetrics) for data reduction and fitting; a scattering pattern recorded from the empty cell was used for background subtraction. Least square fitting was performed starting from the analytical model presented in a previous work of us [24], where catalyst nanoparticles are modelled as a product of a form factor by a structure factor: $I(q) \propto I_P \bullet P(D_P, \sigma_P, q) \bullet S(D_f, \xi, q)$. As, from data fitting, evidence of aggregation was found in the MEA loaded with the Pt catalyst only, in the MEA loaded with the Pt_3Co catalyst nanoparticles, the structure factor was not used, thus catalyst nanoparticles were modelled by using a form factor only. Due to the masking effect introduced by the presence of the GDL, and in agreement with the approximations presented by Gommes and co-workers [24,44] the cross-correlation term was neglected from the model. This assumption allowed to use the analytical model composed by a set of spheres following the Schulz distribution [45,46] as a form factor, to retrieve particle size distribution, expressed in terms of mean particle size (D_P), and its standard deviation (σ_P), scaled by the forwarded scattering probability (I_P). The fractal model developed by Teixeira [47] was used as a structure factor, where the fractal dimension (D_f) is related to the morphology of the cluster shape, while the cut-off distance (ξ) describes the behaviour of the pair correlation function

for larger distances than the size of a catalyst nanoparticle, and can be related to the average cluster size and by means of the calculated radius of gyration $R_g^2 = \xi^2 D_f(D_f+1)/2$ [48]. The catalyst specific Surface Area (SA), $SA = \langle A\rangle/\rho\langle V\rangle$, was calculated as the ratio of the average surface ⟨A⟩ to the average volume ⟨V⟩ of the catalyst nanoparticles [24,49], calculated as the second and third moment of the Schultz probability distribution function [26,50]: $\langle A\rangle = 4\pi\int_0^{R_{max}} f(r)r^2dr$, $\langle V\rangle = \frac{4\pi}{3}\int_0^{R_{max}} f(r)r^3dr$. The Debye-Anderson-Brumberger (DAB) form factor [51,52] was used to model the Vulcan substrate by keeping the correlation length value fixed at 36.07 nm, as previously done [23,24]. A power law was used to model the contribution of the largest structure composing the GDLs, while a Voigt peak [53,54] was used to represent the Nafion ionomer peak. Being the catalyst loading at the anode 16 times lower that the loading at the cathode, and being the catalyst nanoparticles at the anode not expected to evolve as fast as particles at the cathode, their presence was considered negligible.

2.4. SEM-EDX

Cross-sections of the MEAs (razor blade cut) were characterised by Scanning Electron Microscopy (SEM) using a Tescan MIRA III microscope operating at the 30 keV electron beam energy. The EDX spectra were acquired by an SDD EDS spectrometer (JEOL) with 0.98 sr solid angle integrated in JEOL JEM-2200FS microscope. Core loss-edge of Pt, Co, and F were taken in each point in order to obtain the element map of the structure.

2.5. Operando X-ray Photoelectron Spectroscopy (XPS)

Operando XPS measurements were performed using an in-house developed *operando* cell setup [55]. The cell was operated in a half-cell mode, equipped with a Pt counter electrode and Ag/AgCl reference electrode, within a Near-Ambient Pressure XPS (EnviroESCA, SPECS). A monochromatized An Al Kα X-ray source (1484.71 eV, 300 μm spot size), combined with a hemispherical photoelectron analyser (Phoibos 160 NAP 1D-DLD SPECS) was used to acquire the XPS Pt 4f, Au 4f, Co 2p, C1s, O 1 s, F 1 s, and VB spectra with a pass energy set to 20 eV, a measurement step of 0.1 eV, and a dwell time of 0.3 s per point. Spectra were recorded at different applied potentials, with the electron analyser electrically grounded with the working electrode of the *operando* cell.

2.6. Inductively Coupled Plasma Mass Spectrometry (ICP-MS)

The concentrations of Pt and Co were measured using Inductively Coupled Plasma Mass Spectrometry (ICP-MS) with a NexION 350X instrument (PerkinElmer, USA), equipped with an ESI SC Autosampler. To reduce polyatomic ion interferences originating in the plasma, analyses were performed in Kinetic Energy Discrimination (KED) mode with a high-purity helium gas flow rate of 4.8 mL·min^{-1}. Instrument calibration was achieved using a series of standard solutions ranging from 0.2 to 100 μg·L^{-1}, obtained through serial dilution of 10 mg·L^{-1} multielement standards designed for ICP applications (Periodic Table MIX 1 and MIX 2, TraceCERT, Sigma-Aldrich). Quantification of analytes was based on a linear calibration curve within the specified concentration range (0.2–100 μg·L^{-1}, $R^2 = 0.99$). Analytical accuracy was verified using two quality control samples at concentrations of 1 μg·L^{-1} and 10 μg·L^{-1}, prepared from a separate multielement standard not employed in calibration (Multielement Quality Control Standard for ICP, VWR Chemicals). The limits of detection for Co (59 u.m.a.) and Pt (195 u.m.a.) are equal to 0.05 μg·L^{-1} and 0.01 μg·L^{-1} respectively. Measurement precision as repeatability (RSD%) for the analysis was <3 %.

2.7. Operando XAS and SAXS analysis

Operando measurements were performed by following a methodology previously consolidated [23]: after characterising MEAs in ***pristine*** conditions, a ***conditioning*** protocol (T_{cell}: 80 °C; 100 % RH N_2 gas flown at both electrodes at the flow rate Φ: 50 NmL·min^{-1}) was used to properly hydrate the MEAs. Afterwards, the cell was driven by a potentiostat (SP-240, Biologic), equipped with a booster capable of providing a maximum output of 4 A. Once the MEA was properly hydrated, the ***break-in*** procedure was started (T_{cell}: 80 °C; anode: 100 % RH H_2, Φ: 20 NmL·min^{-1}; cathode: 100 % RH O_2, Φ: 20 NmL·min^{-1}), consisting in chrono-amperometry at the potential of 0.4 V for 120 min. During this step SAXS patterns were continuously recorded every ten minutes; XAS spectra were collected during the break-in process only. Finally, an ***AST*** simulating load cycling during FC operation [56] was applied: the AST consisted in switching cell potential between 0.65 V and 0.90 V, with a holding time of three seconds for each step. For the MEA loaded with the Pt catalyst nanoparticles only 4000 cycles could be recorded, while 7000 cycles could be recorded when the Pt_3Co nanoparticles were used as a catalyst. The temporal window of analysis was considered satisfying, as it was previously demonstrated that the most remarkable evolution takes place in the early stages of operation [28]. Every 250 potential cycles, one SAXS pattern and three voltammograms were recorded. Cyclic Voltammetry (CV) was carried out by measuring three voltammograms ranging from 0.05 to 1.0 V at the scan rates of 20, 50, and 100 mV·s^{-1}. The Specific Electrochemically Active Surface Area (ECSA) was calculated as: $ECSA = Q(H_{UPD})/(C \bullet m_{Pt})$, where $Q(H_{UPD})$ represents the Hydrogen Underpotential Deposited Charge (obtained by integrating the current values within the hydrogen desorption region), C is the hydrogen adsorption charge on a smooth Pt electrode (equal to 210 μC·cm^{-2}), and m_{Pt} is the mass of the catalyst loading per unit area ($m_{Pt} = 0.8$ mg·cm^{-2}). Nonetheless, due to the intrinsic limitations in ECSA calculation for Pt-bimetallic alloys [57–60], the specific surface area calculated from SAXS data analyses was used to complementary monitor the ECSA evolution, as previously done [23,24]. After the break-in step and at the end of ASTs, water produced by the fuel cell was sampled for ICP-MS analyses.

Operando SAXS and XAS data were completed by measuring *ex situ* a set of twin MEAs aged by applying the same protocol, stopped at specific time points (pristine conditions and after 1250, 2500 and 5000 cycles). The MEAs loaded with Pt_3Co catalyst were further measured by cross-sectional SEM-EDX.

3. Results and discussion

The two types of MEA were characterised in pristine conditions at first, as shown in Fig. 1 and summarised in Table 1. Nanoparticle size distribution gives rise to the shoulder present at intermediate q-ranges of SAXS patterns (in between 0.6 and 1 nm^{-1}): in Fig. 1a it is evident as Pt_3Co nanoparticles are bigger, as this feature is shifted towards lower q-values. Pt nanoparticles are characterised by smaller, and more monodispersed particle population with a mean particle size (within the Schultz distribution) of 2.28 ± 0.02 nm and distribution width equal to 0.83 ± 0.01 nm, in agreement with results previously obtained [23,24]. Instead, the Pt_3Co nanoparticles are characterised by a mean particle size of 3.55 ± 0.05 nm and a distribution width of 1.49 ± 0.01 nm, in agreement with both other references found in literature [61,62], and with specifications provided by the supplier [63]. The two scattering patterns show a similar evolution at higher q-values (where the contributions from the bigger features characterising the Vulcan support and the GDL are present). Nonetheless, they differ at lower q-values, where the form factor representing the catalyst nanoparticles differently overlaps with the Nafion ionomer peak, which can be found in between

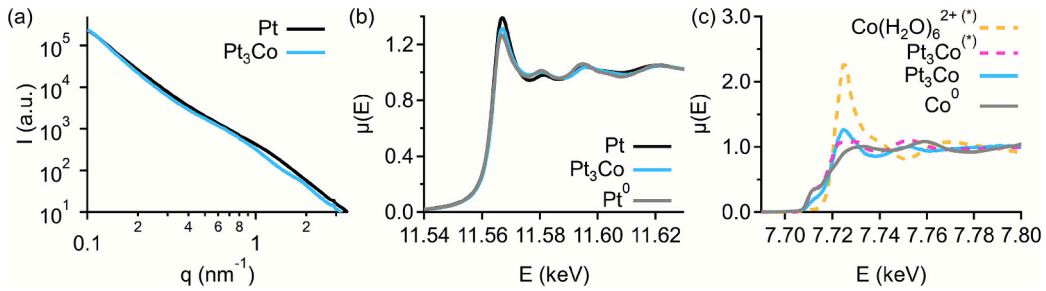

Fig. 1. MEAs characterization in pristine conditions. MEAs loaded with Pt and Pt_3Co catalysts are compared in pristine conditions: (a) SAXS patterns; normalized XANES spectra recorded at (b) the Pt L_3- and (c) Co K- edges, respectively. Continuous lines represent measured data, dashed lines(*) have been replotted from the work of Takao *et al.* [67].

Table 1
MEAs in pristine conditions: quantitative comparison. A comparison of the main results obtained by fitting the SAXS patterns represented in Fig. 1a with the analytical model, by linear combination fitting of the XANES spectra from Fig. 1b and EXAFS refinements (Fig. S1). The main SAXS results are listed in terms of mean particle size (D_P) and standard deviation (σ_P) within the Schultz distribution. The main XANES results are presented in terms of percentage ratio of the amount of Pt in the metallic (Pt^0) and oxidised (Pt^{Z+}) states. From EXAFS refinements of the same spectra (full results in Table S2), the average bond length of the first shell (r) was calculated. Notes: [a] Reference data reported from a previous work [23]. [b] XAS recorded at the Pt L_3-edge. [c] XAS recorded at the Co K-edge; this value is referred to the shell calculated for Co in Pt_3Co, which however is not the only shell used, as to achieve a good EXAFS fit, CoO shell needed to be inserted (in accordance with the results from XANES linear combination fitting on the same sample, reported in Table S1).

	D_P (nm)	σ_P (nm)	Pt^0 (%)	Pt^{Z+} (%)	r (Å)
Pt	2.28 ± 0.02	0.83 ± 0.01	89 ± 3 [a,b]	11 ± 3 [a,b]	2.748 ± 0.003 [a,b]
Pt_3Co	3.55 ± 0.05	1.49 ± 0.01	96 ± 3 [b]	4 ± 3 [b]	2.706 ± 0.009 [b]
					2.685 ± 0.007 [c]

1 and 2 nm^{-1}, depending on the degree of relative humidity at which the ionomer is exposed [64].

When comparing normalized XAS spectra measured at the Pt L_3-edge (Fig. 1b), the overlap of the edge position and the similar intensity of the white lines in the normalized XAS spectra reveal that Pt is mostly present in metallic state for both catalyst compositions. Linear combination fitting analyses of the XANES spectra (Fig. S1a), allowed to estimate the percentage of metallic Pt with respect to the total Pt content. This was found to be equal to 89 ± 3 % when the catalyst was composed of Pt only [23], and to 96 ± 3 % for the Pt_3Co catalyst nanoparticles. This is also summarised in Table 1, where the corresponding fraction of oxidised platinum (Pt^{Z+}) is listed too. The slightly lower oxidation degree detected for Pt_3Co compared to bare Pt catalyst can be attributed to an electronic ligand effect induced by Co incorporation, which leads to charge transfer from Co to Pt and a consequent downward shift of the Pt d-band centre, weakening Pt—O interactions and hence reducing the tendency of Pt to form oxidised species, stabilizing metallic Pt sites. Such a stabilization effect is consistent with the smaller ECSA decay observed for Pt_3Co during ASTs (as it will be later presetned and summarised in Table 2) and agrees with previous reports on Pt–M (M = Co, Ni) alloys, where alloying-induced d-band shifts were shown to lower the Pt—O binding energy and enhance catalyst stability [10–13].

Since an increased white line intensity in the XAS spectra of a mainly metallic Pt sample can be either due to PtO and/or PtO_2 (oxidation state Pt^{2+} and Pt^{4+}, respectively) [65,66], the oxidation state of Pt within the alloy was crosschecked with XPS on a single cathode electrode. The recoded XPS Pt 4f spectrum (Fig. S2a), allowed to determine that the oxidised platinum is in the oxidation state Pt^{2+}. From the analysis of this spectrum, the fraction of oxidised Pt was found to be equal to 16 %, resulting bigger than what obtained *via* XANES linear combination fitting. Such a difference can be related to the limited sensitivity of XPS in probing sample bulk, being this technique more suitable for surface analysis. It follows that the incidence of the intensity related to the oxidised form, located on the nanoparticle surface, is much higher for XPS. The characterization of the pristine Pt_3Co catalyst was completed by XANES linear combination fitting analyses on the spectrum collected at the Co K-edge data (Figs. 1c, S1b, and Table S1) which allowed to estimate a fraction of metallic Co (Co^0) equal to 59 ± 5 % (either bounded to other Co atoms, 6 %, or to Pt ones, 53 %). The remaining Co belongs to the oxidised form, as also suggested from the increased intensity of the white line with respect to the reference metal and Co alloy (Fig. 1c). Interestingly, oxidised Co was found both in the form of CoO (19 ± 3 %) and forming oxide/hydroxide phases, in particular the Co $(H_2O)_6^{2+}$ complex (22 ± 5 %). This finding was unexpected, but partially

Table 2
Summary of combined CV, SAXS, and XAS analysis. Particle size distribution (D_P, σ_P) and geometric surface area (SA), ECSA, relative ratio among metallic and oxidised Pt and Co is compared in pristine conditions, after the break-in, and after 5000 cycles for the compared catalysts for this study. Notes: results from linear combination fit of XAS spectra measured at the Pt L_3-edge in the XANES region are expressed as a ratio among metallic (Pt^0) and oxidised (Pt^{Z+}) platinum, while fit on XAS spectra measured at the Co K-edge are expressed as a ratio of Co in metallic (Co^0) and oxidised (Co^{2+}) states. Co in metallic state is represented by the fraction of Pt_3Co compound used for fitting, while Co in oxidised state is defined by the sum among the fractions of CoO and $Co(H_2O)_6^{2+}$. Detailed results are listed in Table S5. Notes: [a] Reference data reported from a previous work [23].

		D_P (nm)	σ_P (nm)	SA (m^2/g)	ECSA (m^2/g)	Pt^0/Pt^{Z+} (%)	Co^0/Co^{2+} (%)
Pt	Pristine	2.28 ± 0.02	0.83 ± 0.01	30.5	–	89 / 11 (±3) [a]	–
	After break-in	2.32 ± 0.04	0.92 ± 0.01	30.1	31.0	95 / 5 (±2) [a]	–
	After 5000 AST	5.71 ± 0.05	1.54 ± 0.01	12.2	16.7	93 / 7 (±2)	–
Pt_3Co	Pristine	3.55 ± 0.05	1.49 ± 0.01	26.2	–	96 / 4 (±3)	60 / 40 (±4)
	After break-in	2.59 ± 0.03	1.42 ± 0.01	31.9	29.94	98 / 2 (±2)	26 / 74 (±6)
	After 5000 AST	4.28 ± 0.01	2.24 ± 0.01	21.3	19.26	88 / 12 (±3)	74 / 26 (±4)

in agreement with the results presented by Takao and co-workers [67], who also reported the formation of such a complex. EXAFS refinements of the spectra recorded at both the Pt L_3-edge and the Co K-edge (Figs. S1c, and S1d), allowed to quantify the average bond length for the two specimens (*r*, Tables 1 and S2). These results are in agreement with those previously reported by Gilbert and co-workers [61]; in particular, it can be appreciated as the alloying of Pt with Co is decreasing the first shell bond-length.

After MEA conditioning, the break-in step was performed, by operating the fuel cell at 0.4 V; the corresponding time-resolved scattering pattern and XAS spectra (recoded at the end of the break-in procedure) are shown in Fig. 2. As expected, and in agreement with a previous study by the same authors [23], once bare Pt nanoparticles are used as catalyst, no remarkable evolution can be detected, and the main changes in SAXS patterns (Fig. 2a) are related to Nafion hydration, which is reflected on ionomer peak shift towards lower q-values and the increase in intensity [68,69] (as summarised in Fig. S3, where the complete evolution of the parameters composing the model is shown). From fitting the scattering patterns with the analytical model (Fig. 3a), the relative variation detected in particle size was found to be limited to the 1.7 % (2.32 ± 0.04 nm) with respect to the starting value, while standard deviation increased by about 8.7 % (0.92 ± 0.01 nm); consequently, the specific surface area evolution shows no significant changes too (Fig. 3b). In fact, the main effect of the break-in condition can be only noticed in XAS analysis, where the most remarkable difference between the spectra collected in pristine conditions and at the end of the break-in process (Fig. 2b) consist in a small decrease in white line intensity, indicating a partial reduction of the oxidised platinum fraction within the MEA, thanks to the reducing potential applied [70]. Results of the XANES linear combination fitting, revealed and increase in the metallic platinum fraction from 89 ± 3 % to 95 ± 3 %, in agreement with previous observations [23].

Once the same procedure was run on the MEA loaded with the Pt_3Co catalyst (Fig. 2c), Nafion hydration was again spotted in the high-q region of the time-resolved scattering patterns. In addition, slight changes can be also observed at intermediate q-values, where the form factor representing catalyst nanoparticles is present. From fitting the patterns with the analytical model (the complete set of parameters is shown in Fig. S4), the mean particle diameter was found to be decreasing from

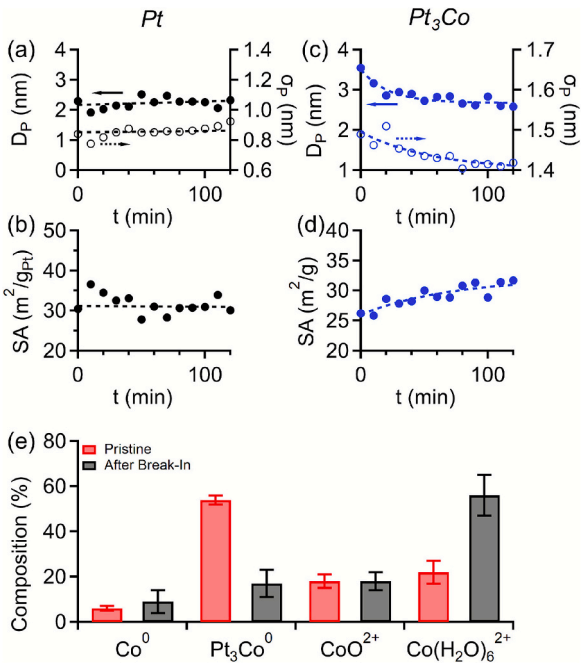

Fig. 3. Quantitative comparison of the effects due to the break-in procedure. Time resolved evolution of mean particle size and distribution width obtained from fitting the SAXS patters recorded during the break-in of the MEA loaded with (a) the bare Pt catalyst (patterns shown in Fig. 2a), and (c) with the Pt_3Co catalyst (patterns shown in Fig. 2c). Corresponding evolution of the specific surface area calculated from SAXS analysis of the MEA loaded with (c) bare Pt, and (d) Pt_3Co catalyst. Dashed lines are guides for the eye only. (e) Results from XANES linear combination fitting performed on the Co K-edge spectra shown in Fig. 2e (results listed in Table S4). Notes: Pt_3Co and Co $(H_2O)_6^{2+}$ fractions were determined using the spectra reported by Takao et al. [67].

3.55 ± 0.04 to 2.59 ± 0.03 nm (reduction of 27.0 %) and the width of the distribution revealed a decrease from 1.49 ± 0.01 nm to 1.42 ± 0.01 nm (reduction of 4.8 %). Consequently, the specific surface area was found to be increasing from 26.2 m^2/g to 31.9 m^2/g (Fig. 3d). Such a

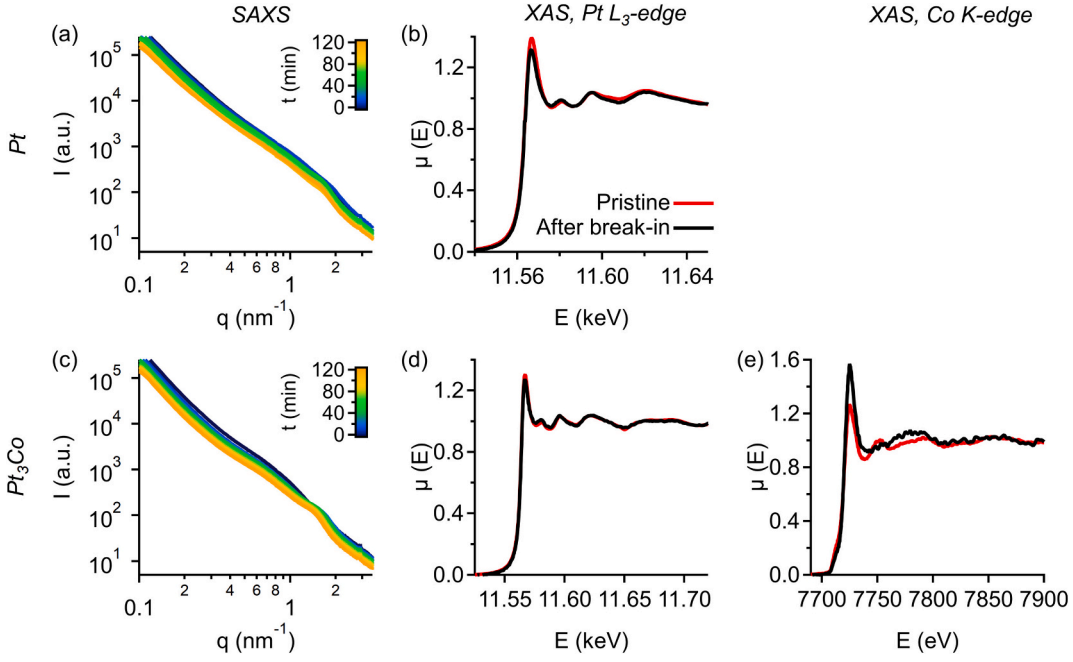

Fig. 2. *Operando* analysis during the break-in procedure. Time resolved evolution of: (a,c) SAXS patterns, and (b,d,e) XAS spectra collected at both (b,d) Pt L_3-edge, and (e) Co K-edge for the two MEA loaded with the bare Pt and Pt_3Co catalysts. SAXS patterns have been vertically shifted for the sake of clarity.

shrink in particle size was assumed to be related to the structural rearrangement induced by Co leaching. This fact was confirmed by ICP-MS analysis performed on the water produced by the fuel cell during break-in, which revealed a Co concentration of 31.0 ± 0.05 μg/L (Table S3). Remarkable changes of Co are visible also in the XANES spectra collected at the Co K-edge (Fig. 2e), where changes in the first oscillations of the EXAFS region are clearly visible in addition to the increase of the white line intensity. Results from linear combination fitting analyses on these spectra (Fig. 3e and Table S4) seems to evidence an increase in the fraction of $Co(H_2O)_6^{2+}$ after the break-in step, which may originate from leaching of Co atoms initially composing the catalyst. On contrary, no remarkable changes are visible in the XAS spectra collected at the Pt L_3-edge (Fig. 2d) which are only characterised by a slight increase in the fraction of metallic Pt (from 95 ± 3 % to 98 ± 3 %), in analogy with what was observed in the MEA loaded with bare Pt only (the less pronounced effect can be primarily related to the lower fraction of oxidised Pt phases in the pristine sample and/or to the lower amount of Pt capable of being oxidised at the sample surface, due to its composition).

After the break-in step, catalyst stability under the AST was compared. Regarding the MEA loaded with bare Pt nanoparticles, by observing the evolution of the shape of the cyclic voltammograms recorded once the AST was applied (Fig. 4a), it is straightforward noticing the reduction of ECSA, as highlighted by the reduction of the area underneath the peaks in the hydrogen desorption region. In parallel, time-resolved SAXS patterns (Fig. 4b) are characterised by the shift of the bump originating from catalyst nanoparticles to lower q-values, indicating an increase in the average particle size. From quantitative analysis of SAXS patterns recorded in *operando* conditions up to 4000 cycles, the mean particle size was found to be increasing from 2.28 ± 0.02 nm (in pristine conditions, Table 1) to the final value of 6.21 ± 0.03 nm (Figs. 5a; complete SAXS results are shown in Fig. S5), with the most predominant evolution taking place within 3000 cycles. In the same timeframe, distribution width was found to increase (σ_p, Figs. 5a) while specific surface area was reducing (SA, Figs. 5b) from 30.11 m^2/g_{Pt}, 11.61 m^2/g_{Pt} after 4000 cycles, representing a reduction of 38.6 % with respect the initial value before starting ASTs. These results have been confirmed by measuring *ex situ* a second set of twin MEAs, which aging ended at specific time points (1250, 2500 and 5000 cycles, Fig. S6). ECSA was calculated from cyclic voltammograms, revealing a 53.8 % reduction, from 30.95 m^2/g_{Pt} to 16.67 m^2/g_{Pt}. As also observed in a previous study by the authors [23], ECSA reduction is more pronounced with respect the reduction of the geometrical specific surface area retrieved by SAXS. Nonetheless this may be attributable to the disconnection of catalyst nanoparticles from both the mass- and charge-transport conduction paths within the catalyst layer upon catalyst aging. Again, by means of XANES linear combination fitting analyses on spectra collected *ex situ* on the MEA aged up to 5000 cycles (Fig. 4c), in analogy to results previously achieved [23], the growth of the catalyst nanoparticle size was found to be correlated to the increase in the metallic Pt fraction (up to 93 ± 2 %) with respect to pristine conditions. Nonetheless, no remarkable variation in catalyst composition with respect the beginning of ASTs was observed. It is worth noticing that this value is lower than the value recorded after break-in and could be due to oxide formation under voltage cycling.

While for the bare Pt catalyst nanoparticles, aging is evolving within the first few thousand cycles mainly, a different behaviour was observed on the Pt_3Co catalyst. In fact, voltammogram evolution shows less pronounced changes in the hydrogen desorption region, and the most remarkable changes involve the shift to upper voltages of the reduction peak of platinum (Figs. 4d). SAXS scattering pattern evolve analogously to the previous sample, with the bump representing the catalyst nanoparticle population shifting towards lower q-values (Fig. 4e). From fitting time resolved patterns (Fig. 5c, full results in Fig. S7) nanoparticle size growth was quantified starting from 2.59 ± 0.03 nm, to 4.28 ± 0.09 nm (after 5000 cycles), up to 6.14 ± 0.09 nm after 7000 cycles, with the distribution width increasing from 1.42 ± 0.01 nm, to 2.24 ± 0.01 nm (5000 cycles), up to 2.33 ± 0.02 nm after 7000 cycles. These results were confirmed from *ex situ* measurements of a twin set of the MEAs whose aging was stopped at specific time points (1250, 2500, and 5000 AST cycles, Fig. 5c, Fig. 5d, and Fig. S8). Aging was found to follow a three-step evolution: on a first step (up to 500–750 cycles) the mean particle size is apparently constant, with only an increase in the distribution width. Afterwards, the particle size starts to increase slightly, accompanied by a decrease in the geometric surface area (Fig. 5d). This step lasts until about 2500 cycles, and it is followed by the final step, characterised by accelerated mean particle size growth (and a concomitant decrease in the specific geometrical surface area). A similar process was previously spotted by the same authors when studying the *in*

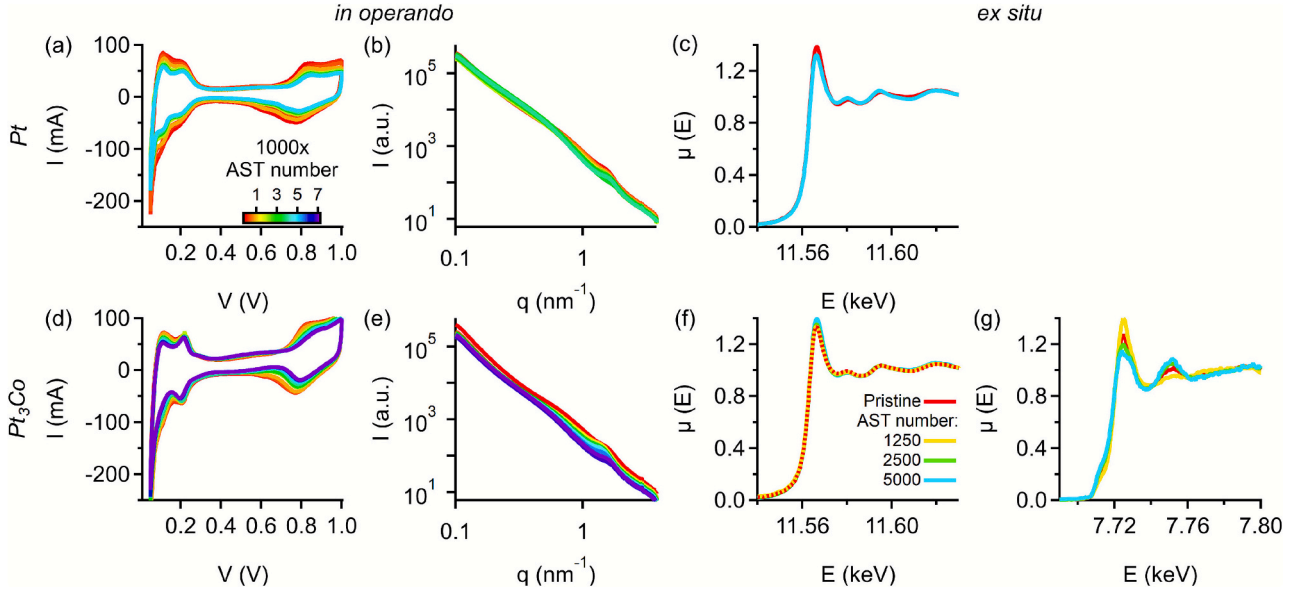

Fig. 4. *Operando* and *ex situ* evolution during ASTs. *Operando* time resolved evolution of (a,d) cyclic voltammograms, (b,e) scattering patterns while ASTs were applied for 4000 cycles for the MEA loaded with the Pt catalyst and for 5000 cycles for the MEA hosting the Pt_3Co catalysts nanoparticles. *Ex situ* spectra collected (c, f) at the Pt L_3-edge and (g) at the Co K-edge of MEA singularly aged and stopped at key time-points: pristine conditions and after 5000 cycles for the MEA hosting Pt nanoparticles, while pristine conditions, and after 1250, 2500, and 5000 cycles were compared for the MEA loading the Pt_3Co nanoparticles.

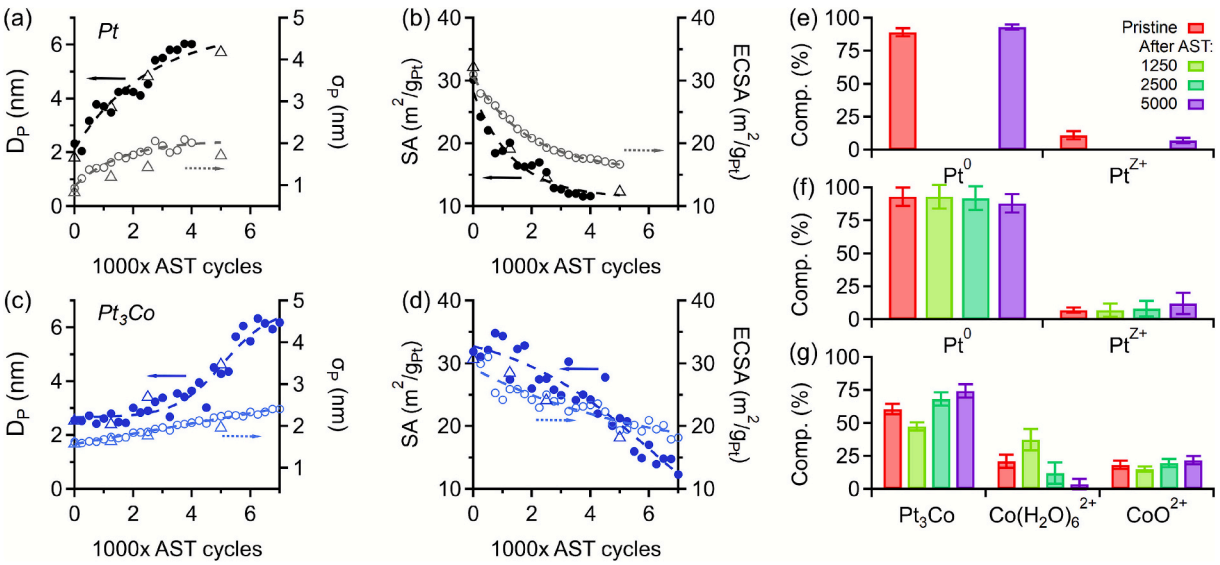

Fig. 5. ASTs: quantitative comparison. Time-resolved evolution of the mean particle size and standard deviation within the Shultz distribution retrieved from the MEAs loaded with the bare Pt (a, b) and Pt_3Co (c, d) catalyst nanoparticles (obtained from fitting scattering patterns represented in Fig. 4b and Fig. 4e respectively). Corresponding time-resolved evolution of the specific SA calculated from SAXS analysis and ECSA calculated from the voltammograms measured every 250 cycles for the two types of MEA (Fig. 4a and Fig. 4d). Dashed lines are guides for the eye only. Triangles represent results from MEAs measured *ex situ via* SAXS, after being aged at specific time points. In Figures (e) to (g) results from linear combination fitting of the XANES spectra collected *ex situ* from the MEAs are reported. (e) Bare-Pt catalyst nanoparticles at the Pt L_3-edge, (f) Pt_3Co catalyst nanoparticles at the Pt L_3-edge, and (g) Pt_3Co catalyst nanoparticles at the Co K-edge. Results from linear combination fitting are listed in Tables S1 and S3.

situ aging of $Pt_XNi_{(1-X)}$ bimetallic alloy to be used as a catalyst for the ORR [17]: there, the first step identified was Ni dissolution being the predominant degradation phenomena at the early stages of catalyst degradation, followed by particle coalescence, to end with Ostwald ripening [17]. The establishment of Ostwald ripening as the main degradation process on a later stage was also reported on a bare Pt catalyst by Martens and co-workers [28]. Here, we claim that a similar degradation process is taking place, even if driven by different kinetics, due to the different catalyst composition and operational environment. More in depth, the skewness evolution of the number-weighted size distribution retrieved from SAXS data analysis (Fig. S9), suggests that the prevalence of Ostwald ripening over additional degradation phenomena can be spotted after 3000 cycles, when skewness starts to decrease, as previously observed [17]. In contrast to the bare Pt nanoparticles, it is worth to underline as the growth rate of the particle population seems to stabilize after 6000 cycles. The SA decrease follows a quasi-linear trend. In contrast to the observations made on the bare Pt catalyst, the calculated ECSA showed a slight linear decline. Nonetheless, due to the general uncertainty characterising ECSA calculations for Pt_3Co catalysts [57–60], the evolution of SA could be in this case considered as a more reliable marker. Such a picture is supported by the *ex situ* XAS measurements carried out on the differently aged twin MEAs. In fact, spectra measured at the Pt L_3-edge do not show remarkable changes (Fig. 4f), even if (very interestingly, and in contrast with what was detected on the MEA loaded with bare Pt catalyst), a very slight trend of Pt oxidation can be detected by the gradual decrease of the white line intensity, as also confirmed from linear combination fitting where a slight increase in the fraction of oxidised Pt from 7 % to 12 % was obtained (Table S5). These results were further confirmed by applying the same stress test to the single cathode electrode in *operando* XPS analysis. In fact, by applying a stable potential (1.5 V, Fig. S2b), as well as by running the same stress test (for 50 cycles, Fig. S2c), the oxidised Pt content was found growing from the 16 % to the 18 % in the former case, and up to 23 % when AST were applied (while cycling it was found that the overall fraction of oxidised Pt is composed by a fraction of Pt^{2+} and a fraction of highly oxidised Pt), corresponding to an increase of the overall fraction of oxidised Pt equal to 7 %. Small but unavoidable Pt dissolution might be in this way the cause of the minor increase of the fraction of oxidised Pt observed when measuring XAS spectra at the Pt L_3-edge (Fig. 5f). Nonetheless, by sampling waters produced by fuel cell operation after ASTs no Pt nor Co traces could be detected and hence, if present, their concentration should be lower than 0.01 μg/L for Pt and 0.05 μg/L for Co, corresponding to the instrumental limit of the ICP-MS used (Table S3).

The MEAs were further measured at the Co K-edge: as shown in Fig. 4g, a non-linear trend was detected: an initial increase in the fraction of oxidised Co can be observed after the first 1250 cycles, followed by a significant reduction in oxidised Co content, as underlined by the reduced white line intensity. From the XANES linear combination fitting analyses (Fig. 5g and Table S5), it can be noticed that after the first 1250 cycles the fraction of Co atoms still bounded to Pt atoms is decreased, whereas the fraction of hydrated Co atoms is increased, suggesting ongoing Co leaching. In fact, it was demonstrated that Co atoms tend to migrate from the bulk of the nanoparticles towards the surface [71], where Co leaching is expected to take place. It is reasonable to conclude that the increase in the fraction of the hydrated Co atoms (Fig. 5g and Table S5) within the first 1250 cycles is connected with oxidation of Co atoms migrating from the bulk to the particle surface, which would further dissolve after the formation of the Pt-rich skin [20,71]. Afterwards, the progressive reduction of the remaining Co^{2+} (as observed in the spectra collected after 2500 and 5000 cycles) could also be an effect due to the fact that the only Co still present in the cathode is strongly bounded within the Pt_3Co alloy at the core of the nanoparticles, beneath the Pt-rich skin. While NAP-XPS was unable to provide additional information due to the low amount of Co present in the sample surface (Figs. S2d, S2e, and S2f), cross-sectional SEM-EDX analyses (Fig. 6) shows that Co leaches in the electrolyte (reaching the anode in some cases) also during the stress test, as previously observed [72]. Such a loss was also confirmed by the decreasing trend characterising the calculated Co-to-Pt atomic concentration calculated from EDX (Fig. 6e). A further evidence for Co leaching can also be obtained by comparing the *ex situ* XAS spectra as collected (not normalized) of samples in pristine state and after ASTs (Fig. S10), where a clear decrease in the absorption edge-step can be observed.

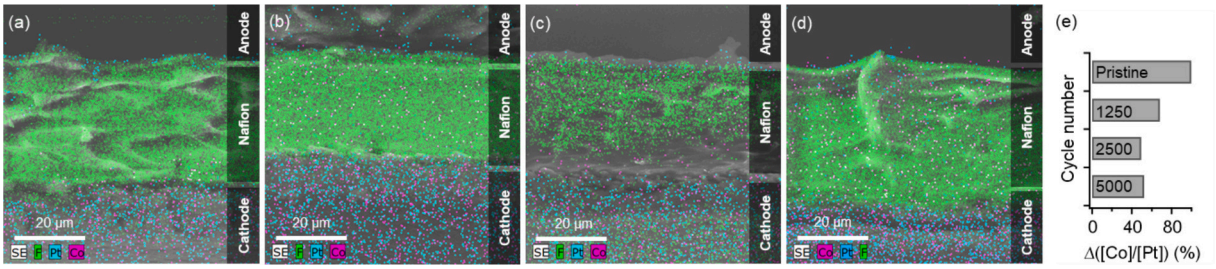

Fig. 6. SEM-EDX. Cross-sectional SEM with EDX of the MEA loaded with the Pt_3Co catalyst obtained from the MEA measured *ex situ* with both SAXS (Fig. S6) and XAS (Fig. 4). (a) MEA in pristine conditions. The other three MEAs were cycled for (b) 1250, (c) 2500, and (d) 5000 AST cycles. Scale bar: 20 µm; colour code: green represents fluorine, light blue represents platinum, and magenta represents cobalt. (e) Relative variation of the Co-to-Pt atomic concentration ratio calculated from EDX with respect to pristine conditions. (For interpretation of the references to colour in this figure legend, the reader is referred to the web version of this article.)

4. Conclusions

In this work, the stability of two benchmark formulation of catalyst materials for the ORR in PEMFC was tested under an AST mimicking load cycling operation. Time-resolved, *operando* electrochemical data were complemented by the analysis of *operando* SAXS patterns, *operando* XAS spectra and *ex situ* SAXS, and XAS measurements conducted on a set of twin MEAs aged by using the same protocol. For the MEAs loaded with Pt_3Co, *operando* NAP-XPS and SEM-EDX were used to complement results, while ICP-MS was used to quantify traces of dissolved metals into water produced by the fuel cell. Catalyst evolution was depicted starting from pristine conditions, after the break-in step, and finally under ASTs; main results are summarised in Table 2. Catalyst evolution dynamics were found to differ depending on the catalyst formulation. In particular, bare Pt catalyst was found to be stable during the break-in step, and that the loss of ECSA observable while ASTs are applied is related with both an increase in particle size, and to a slight decrease in the ratio between the fraction of metallic-to-oxidised Pt. In particular, catalyst degradation was found to be more pronounced within the first 3000 cycles and to further stabilize at a final value between 3000 and 4000 cycles. On the contrary, the catalyst composed by the Pt_3Co nanoparticles, was found to be strongly affected by Co leaching during the break-in step. The resulting formation of a Pt-rich skin helped to slow down the particle size growth, which mostly evolved in the range between 3000 and 6000 cycles. The continuous leaching of Co from the sample was confirmed by both XAS and SEM-EDX, as well as by ICP-MS analyses on waters produced by the fuel cell. The ability to properly control leaching in bimetallic catalyst materials, might be the key to mitigate degradation over time.

CRediT authorship contribution statement

Marco Bogar: Writing – review & editing, Writing – original draft, Visualization, Validation, Methodology, Investigation, Formal analysis, Data curation, Conceptualization. **Yurii Yakovlev:** Writing – review & editing, Writing – original draft, Validation, Methodology, Investigation, Formal analysis, Data curation, Conceptualization. **Simone Pollastri:** Writing – review & editing, Writing – original draft, Validation, Methodology, Investigation, Formal analysis, Data curation, Conceptualization. **Tomáš Hrbek:** Writing – review & editing, Data curation. **David Kalabis:** Writing – review & editing, Data curation. **Giovanna Marussi:** Writing – review & editing, Data curation. **Matteo Crosera:** Writing – review & editing. **Roberto Biagi:** Writing – review & editing, Resources. **Heinz Amenitsch:** Writing – review & editing, Supervision, Resources. **Rodolfo Taccani:** Supervision, Resources. **Iva Matolínová:** Writing – review & editing, Supervision, Resources, Project administration.

Declaration of competing interest

The authors declare that they have no known competing financial interests or personal relationships that could have appeared to influence the work reported in this paper.

Acknowledgments

All of the authors acknowledge the CERIC-ERIC Consortium for the access to experimental facilities and the financial support (proposal 20222217 scheduled at the SAXS beamline). Data at the XAFS beamline were collected during the experiment proposal 20220525.

This work was supported by the project "The Energy Conversion and Storage", funded as project No. CZ.02.01.01/00/22_008/0004617 by Programme Johannes Amos Comenius, call Excellent Research, Ministry of Education, Youth and Sports of the Czech Republic.

M.B. and R.T. acknowledge the financial support from the project sHYpS (sustainable HYdrogen powered Shipping, Horizon Europe call Horizon-CL5-2021-D5-01) and the Italian Operative Program for Research and Innovation 2014–2020 provided by the Italian Ministry of University and Research.

S.P. and R.B. acknowledge the National Recovery and Resilience Plan (NRRP), Mission 04 Component 2 Investment 1.5 – NextGenerationEU, Call for tender n. 3277 dated 30/12/2021 Award Number: 0001052 dated 23/06/2022. S.P. also acknowledge Dr. Luca Olivi and Riccardo Grisonich for their help during the experiment at XAFS.

Appendix A. Supplementary data

Supplementary data to this article can be found online at https://doi.org/10.1016/j.cejgas.2025.100017.

Data availability

Data used for supporting this work are available on a Zenodo repository, which is reachable by the following link: Doi: https://doi.org/10.5281/zenodo.16880902

References

[1] U. Department of Energy Hydrogen, F. Cell Technologies Office, Hydrogen and Fuel Cell Technologies Office Multi-Year Program Plan: Hydrogen Infrastructure, (2024). https://www.hydrogen.energy.gov/library/roadmaps-vision/clean-hydrogen-strategy-roadmap. (accessed June 9, 2025).

[2] L. Fan, H. Deng, Y. Zhang, Q. Du, D.Y.C. Leung, Y. Wang, K. Jiao, Towards ultralow platinum loading proton exchange membrane fuel cells, Energ. Environ. Sci. 16 (2023) 1466–1479, https://doi.org/10.1039/D2EE03169H.

[3] Y. Wang, D.F. Ruiz Diaz, K.S. Chen, Z. Wang, X.C. Adroher, Materials, technological status, and fundamentals of PEM fuel cells – a review, Mater. Today 32 (2020) 178–203, https://doi.org/10.1016/j.mattod.2019.06.005.

[4] M. Grandi, S. Rohde, D.J. Liu, B. Gollas, V. Hacker, Recent advancements in high performance polymer electrolyte fuel cell electrode fabrication – novel materials and manufacturing processes, J. Power Sources 562 (2023) 232734, https://doi.org/10.1016/j.jpowsour.2023.232734.

[5] S. Mo, L. Du, Z. Huang, J. Chen, Y. Zhou, P. Wu, L. Meng, N. Wang, L. Xing, M. Zhao, Y. Yang, J. Tang, Y. Zou, S. Ye, Recent advances on PEM fuel cells: from key materials to membrane electrode assembly, Electrochem. Energy Rev. 6 (2023) 28, https://doi.org/10.1007/s41918-023-00190-w.

[6] J. Yu, C. Su, L. Shang, T. Zhang, Single-atom-based oxygen reduction reaction catalysts for proton exchange membrane fuel cells: Progress and perspective, ACS Nano 17 (2023) 19514–19525, https://doi.org/10.1021/acsnano.3c06522.

[7] M. Escudero-Escribano, K.D. Jensen, A.W. Jensen, Recent advances in bimetallic electrocatalysts for oxygen reduction: design principles, structure-function relations and active phase elucidation, Curr. Opin. Electrochem. 8 (2018) 135–146, https://doi.org/10.1016/j.coelec.2018.04.013.

[8] N. Ishiguro, S. Kityakarn, O. Sekizawa, T. Uruga, T. Sasabe, K. Nagasawa, T. Yokoyama, M. Tada, Rate enhancements in structural transformations of Pt-co and Pt-Ni bimetallic cathode catalysts in polymer electrolyte fuel cells studied by in situ time-resolved X-ray absorption fine structure, J. Phys. Chem. C 118 (2014) 15874–15883, https://doi.org/10.1021/jp504738p.

[9] H.Y. Kim, J.M. Kim, Y. Ha, J. Woo, A. Byun, T.J. Shin, K.H. Park, H.Y. Jeong, H. Kim, J.Y. Kim, S.H. Joo, Activity origin and multifunctionality of Pt-based intermetallic nanostructures for efficient Electrocatalysis, ACS Catal. 9 (2019) 11242–11254, https://doi.org/10.1021/acscatal.9b03155.

[10] V.R. Stamenkovic, B. Fowler, B.S. Mun, G. Wang, P.N. Ross, C.A. Lucas, N.M. Markovic, Improved oxygen reduction activity on Pt3Ni(111) via increased surface site availability, Science (80-.). 315 (2007) 493–497. Doi: https://doi.org/10.1126/science.1135941.

[11] V. Stamenkovic, B.S. Mun, K.J.J. Mayrhofer, P.N. Ross, N.M. Markovic, J. Rossmeisl, J. Greeley, J.K. Nørskov, Changing the activity of electrocatalysts for oxygen reduction by tuning the surface electronic structure, Angew. Chemie - Int. Ed. 45 (2006) 2897–2901, https://doi.org/10.1002/anie.200504386.

[12] J. Greeley, I.E.L. Stephens, A.S. Bondarenko, T.P. Johansson, H.A. Hansen, T. F. Jaramillo, J. Rossmeisl, I. Chorkendorff, J.K. Nørskov, Alloys of platinum and early transition metals as oxygen reduction electrocatalysts, Nat. Chem. 1 (2009) 552–556, https://doi.org/10.1038/nchem.367.

[13] M. Oezaslan, F. Hasché, P. Strasser, Oxygen Electroreduction on PtCo 3, PtCo and Pt 3 Co Alloy Nanoparticles for Alkaline and Acidic PEM Fuel Cells, J. Electrochem. Soc. 159 (2012) B394–B405. Doi: https://doi.org/10.1149/2.075204jes.

[14] J.M. Edjokola, M. Bogar, M. Grandi, R. Taccani, H. Amenitsch, M. Marinšek, V. Hacker, M. Bodner, Humidity-induced degradation mapping of Pt 3 co ORR catalyst for PEFC by in-operando electrochemistry and ex situ SAXS, Small 20 (2024), https://doi.org/10.1002/smll.202407591.

[15] L. Dubau, M. Lopez-Haro, L. Castanheira, J. Durst, M. Chatenet, P. Bayle-Guillemaud, L. Guétaz, N. Caqué, E. Rossinot, F. Maillard, Probing the structure, the composition and the ORR activity of Pt3Co/C nanocrystallites during a 3422h PEMFC ageing test, Appl. Catal. Environ. 142–143 (2013) 801–808, https://doi.org/10.1016/j.apcatb.2013.06.011.

[16] I. Khalakhan, M. Bogar, M. Vorokhta, P. Kúš, Y. Yakovlev, M. Dopita, D.J. S. Sandbeck, S. Cherevko, I. Matolínová, H. Amenitsch, Evolution of the PtNi bimetallic alloy fuel cell catalyst under simulated operational conditions, ACS Appl. Mater. Interfaces 12 (2020) 17602–17610, https://doi.org/10.1021/acsami.0c02083.

[17] M. Bogar, Y. Yakovlev, D.J.S. Sandbeck, S. Cherevko, I. Matolínová, H. Amenitsch, I. Khalakhan, Interplay among Dealloying, Ostwald ripening, and coalescence in PtXNi100-XBimetallic alloys under fuel-cell-related conditions, ACS Catal. 11 (2021) 11360–11370, https://doi.org/10.1021/acscatal.1c01111.

[18] X. Tuaev, S. Rudi, V. Petkov, A. Hoell, P. Strasser, In situ study of atomic structure transformations of Pt-Ni nanoparticle catalysts during electrochemical potential cycling, ACS Nano 7 (2013) 5666–5674, https://doi.org/10.1021/nn402406k.

[19] N. Ishiguro, S. Kityakarn, O. Sekizawa, T. Uruga, H. Matsui, M. Taguchi, K. Nagasawa, T. Yokoyama, M. Tada, Kinetics and mechanism of redox processes of Pt/C and Pt3Co/C cathode Electrocatalysts in a polymer electrolyte fuel cell during an accelerated durability test, J. Phys. Chem. C 120 (2016) 19642–19651, https://doi.org/10.1021/acs.jpcc.6b04437.

[20] L. Dubau, F. Maillard, M. Chatenet, J. André, E. Rossinot, Nanoscale compositional changes and modification of the surface reactivity of Pt3Co/C nanoparticles during proton-exchange membrane fuel cell operation, Electrochim. Acta 56 (2010) 776–783, https://doi.org/10.1016/j.electacta.2010.09.038.

[21] Y. Xiong, L. Xiao, Y. Yang, F.J. Disalvo, H.D. Abruña, High-loading intermetallic Pt3Co/C Core-Shell nanoparticles as enhanced activity Electrocatalysts toward the oxygen reduction reaction (ORR), Chem. Mater. 30 (2018) 1532–1539, https://doi.org/10.1021/acs.chemmater.7b04201.

[22] F. Hasché, M. Oezaslan, P. Strasser, Activity, stability, and degradation mechanisms of Dealloyed PtCu 3 and PtCo 3 nanoparticle fuel cell catalysts, ChemCatChem 3 (2011) 1805–1813, https://doi.org/10.1002/cctc.201100169.

[23] M. Bogar, Y. Yakovlev, S. Pollastri, R. Biagi, H. Amenitsch, R. Taccani, I. Matolínová, Capabilities of a novel electrochemical cell for operando XAS and SAXS investigations for PEM fuel cells and water electrolysers, J. Power Sources 615 (2024) 235070, https://doi.org/10.1016/j.jpowsour.2024.235070.

[24] M. Bogar, Y. Yakovlev, J. Nováková, A.M. Darabut, M. Kriechbaum, H. Amenitsch, R. Taccani, I. Matolínová, A small angle X-ray scattering approach for investigating fuel cell catalyst degradation for both ex situ and in operando analyses, Int. J. Hydrogen Energy 58 (2024) 1673–1681, https://doi.org/10.1016/j.ijhydene.2024.01.261.

[25] T. Asset, C.J. Gommes, J. Drnec, P. Bordet, R. Chattot, I. Martens, J. Nelayah, N. Job, F. Maillard, L. Dubau, Disentangling the degradation pathways of highly defective PtNi/C nanostructures - an operando wide and small angle X-ray scattering study, ACS Catal. 9 (2019) 160–167, https://doi.org/10.1021/acscatal.8b02665.

[26] J. Tillier, T. Binninger, M. Garganourakis, A. Patru, E. Fabbri, T.J. Schmidt, O. Sereda, Electrochemical flow-cell setup for in situ X-ray investigations, J. Electrochem. Soc. 163 (2016) H913–H920, https://doi.org/10.1149/2.0211610jes.

[27] I. Martens, A. Vamvakeros, R. Chattot, M.V. Blanco, M. Rasola, J. Pusa, S.D. M. Jacques, D. Bizzotto, D.P. Wilkinson, B. Ruffmann, S. Heidemann, V. Honkimäki, J. Drnec, X-ray transparent proton-exchange membrane fuel cell design for in situ wide and small angle scattering tomography, J. Power Sources 437 (2019), https://doi.org/10.1016/j.jpowsour.2019.226906.

[28] I. Martens, R. Chattot, J. Drnec, Decoupling catalyst aggregation, ripening, and coalescence processes inside operating fuel cells, J. Power Sources 521 (2022) 230851, https://doi.org/10.1016/j.jpowsour.2021.230851.

[29] H. Matsui, N. Maejima, N. Ishiguro, Y. Tan, T. Uruga, O. Sekizawa, T. Sakata, M. Tada, Operando XAFS imaging of distribution of Pt cathode catalysts in PEFC MEA, Chem. Rec. 19 (2019) 1380–1392, https://doi.org/10.1002/tcr.201800123.

[30] Z. Qiao, C. Wang, C. Li, Y. Zeng, S. Hwang, B. Li, S. Karakalos, J. Park, A.J. Kropf, E.C. Wegener, Q. Gong, H. Xu, G. Wang, D.J. Myers, J. Xie, J.S. Spendelow, G. Wu, Atomically dispersed single iron sites for promoting Pt and Pt 3 co fuel cell catalysts: performance and durability improvements, Energ. Environ. Sci. 14 (2021) 4948–4960, https://doi.org/10.1039/D1EE01675J.

[31] S. Luan, J. Liu, S. Li, S. Li, Z. Lou, M. Lv, X. Cui, L. Jiang, Unveiling the synergistic effect of metal/nitrogen-doped carbon and Pt3Co nanoclusters for boosting the oxygen reduction reaction in PEMFC, Chem. Eng. J. 503 (2025) 158666, https://doi.org/10.1016/j.cej.2024.158666.

[32] H. Wang, J. Liu, K. Du, X. Wang, X. Li, Y. Liu, C. Min, F. Liu, X. Yang, Highly durable ORR catalysts derived from Pt3Co intermetallic nanoparticles and porous carbon modified with CeO2 nanocrystals, J. Power Sources 616 (2024), https://doi.org/10.1016/j.jpowsour.2024.235127.

[33] R. Chattot, C. Roiron, K. Kumar, V. Martin, C.A. Campos Roldan, M. Mirolo, I. Martens, L. Castanheira, A. Viola, R. Bacabe, S. Cavaliere, P.Y. Blanchard, L. Dubau, F. Maillard, J. Drnec, Break-In Bad, On the conditioning of fuel cell Nanoalloy catalysts, ACS Catal. 12 (2022) 15675–15685, https://doi.org/10.1021/acscatal.2c04495.

[34] Y.V. Yakovlev, Y.V. Lobko, M. Vorokhta, J. Nováková, M. Mazur, I. Matolínová, V. Matolín, Ionomer content effect on charge and gas transport in the cathode catalyst layer of proton-exchange membrane fuel cells, J. Power Sources 490 (2021), https://doi.org/10.1016/j.jpowsour.2021.229531.

[35] Y.V. Yakovlev, M.G. Rodríguez, Y.V. Lobko, M. Vorokhta, P. Kúš, I. Matolínová, V. Matolín, Characterization of gas diffusion layer transport properties by limiting current approach, Electrochim. Acta 404 (2022) 139755, https://doi.org/10.1016/j.electacta.2021.139755.

[36] A. Di Cicco, G. Aquilanti, M. Minicucci, E. Principi, N. Novello, A. Cognigni, L. Olivi, Novel XAFS Capabilities at ELETTRA Synchrotron Light Source, in: J. Phys. Conf. Ser., Institute of Physics Publishing, 2009. Doi: https://doi.org/10.1088/1742-6596/190/1/012043.

[37] G. Agostini, D. Cirrincione, M. Antonelli, G. Aquilanti, G. Bertuccio, G. Cautero, F. Ficorella, D. Giuressi, F. Mele, R.H. Menk, L. Olivi, G. Orzan, G. Pepponi, A. Picciotto, A. Rachevski, I. Rashevskaya, L. Stebel, G. Zampa, N. Zampa, N. Zorzi, A. Vacchi, Advanced X-ray PIxel Detector (AXPiDe v2.0): New modular multichannel detector based on SDD available at the XAFS beamline of Elettra, J. Phys. Conf. Ser. 3010 (2025) 6–12. Doi: https://doi.org/10.1088/1742-6596/3010/1/012142.

[38] S. Pollastri, M. Bogar, R. Fiala, H. Amenitsch, Y. Yakovlev, A. Lavacchi, G. Aquilanti, V. Matolin, Characterization of innovative Pt-ceria catalysts for PEMFC by means of ex-situ and operando X-ray absorption spectroscopy, Int. J. Hydrogen Energy 47 (2022) 8799–8810, https://doi.org/10.1016/j.ijhydene.2021.12.241.

[39] B. Ravel, M. Newville, Athena, Artemis, HEPHAESTUS: data analysis for X-ray absorption spectroscopy using IFEFFIT, in: J. Synchrotron Radiat., 2005: pp. 537–541. Doi: https://doi.org/10.1107/S0909049505012719.

[40] R.W.G.Wtckoff, Crystal Structures Volume 1, American Mineralogist Crystal Structure Database, 1963.

[41] A.H. Geisler, D.L. Martin, A new superlattice in co-Pt alloys, J. Appl. Phys. 23 (1952) 375, https://doi.org/10.1063/1.1702216.

[42] H. Amenitsch, M. Rappolt, M. Kriechbaum, H. Mio, P. Laggner, S. Bernstorff, First performance assessment of the small-angle X-ray scattering beamline at ELETTRA, J. Synchrotron Radiat. 5 (1998) 506–508, https://doi.org/10.1107/S090904959800137X.

[43] M. Burian, C. Meisenbichler, D. Naumenko, H. Amenitsch, SAXSDOG: open software for real-time azimuthal integration of 2D scattering images, J. Appl. Cryst. 55 (2022) 677–685, https://doi.org/10.1107/S1600576722003685.

[44] C.J. Gommes, T. Asset, J. Drnec, Small-angle scattering by supported nanoparticles: exact results and useful approximations, J. Appl. Cryst. 52 (2019) 507–519, https://doi.org/10.1107/S1600576719003935.

[45] M. Kotlarchyk, S.H. Chen, Analysis of small angle neutron scattering spectra from polydisperse interacting colloids, J. Chem. Phys. 79 (1983) 2461–2469, https://doi.org/10.1063/1.446055.

[46] M. Kotlarchyk, R.B. Stephens, J.S. Huang, Study of Schultz distribution to model polydispersity of microemulsion droplets, J. Phys. Chem. 92 (1988) 1533–1538, https://doi.org/10.1021/j100317a032.

[47] J. Teixera, Small-Angle Scattering by Fractal Systems, 1988.

[48] C.M. Sorensen, G.M. Wang, Size distribution effect on the power law regime of the structure factor of fractal aggregates, Phys. Rev. E - Stat. Physics, Plasmas, Fluids, Relat. Interdiscip. Top. 60 (1999) 7143–7148. Doi: https://doi.org/10.1103/PhysRevE.60.7143.
[49] M. Povia, J. Herranz, T. Binninger, M. Nachtegaal, A. Diaz, J. Kohlbrecher, D. F. Abbott, B.J. Kim, T.J. Schmidt, Combining SAXS and XAS to study the operando degradation of carbon-supported Pt-nanoparticle fuel cell catalysts, ACS Catal. 8 (2018) 7000–7015, https://doi.org/10.1021/acscatal.8b01321.
[50] J.W. Bullard, Q. Jin, K.A. Snyder, How do specific surface area and particle size distribution change when granular media dissolve? Chem. Eng. J. 406 (2021) https://doi.org/10.1016/j.cej.2020.127098.
[51] P. Debye, A.M. Bueche, Scattering by an inhomogeneous solid, J. Appl. Phys. 20 (1949) 518–525, https://doi.org/10.1063/1.1698419.
[52] P. Debye, H.R. Anderson, H. Brumberger, Scattering by an inhomogeneous solid. II. The correlation function and its application, J. Appl. Phys. 28 (1957) 679–683, https://doi.org/10.1063/1.1722830.
[53] B.H. Armstrong, Spectrum line profiles: the Voigt function, J. Quant. Spectrosc. Radiat. Transf. 7 (1967) 61–88, https://doi.org/10.1016/0022-4073(67)90057-X.
[54] E.E. Whiting, An empirical approximation to the Voigt profile, J. Quant. Spectrosc. Radiat. Transf. 8 (1968) 1379–1384, https://doi.org/10.1016/0022-4073(68)90081-2.
[55] T. Hrbek, P. Kúš, M.G. Rodríguez, V. Matolín, I. Matolínová, Operando X-ray photoelectron spectroscopy cell for water electrolysis: a complete picture of iridium electronic structure during oxygen evolution reaction, Int. J. Hydrogen Energy 57 (2024) 187–197, https://doi.org/10.1016/j.ijhydene.2023.12.216.
[56] T. Abdel-Baset, T. Benjamin, R. Borup, K.E. Martin, N. Garland, S. Hirano, J. Kopasz, B. Lakshmanmn, D. Masten, M. Mehall, D. Myers, D. Papageorgopoulos, W. Podolski, T. Trabold, B. Vermeersch, J. Waldecker, The. US Deparment of Energy (DOE). Energy Efficiency and Renewable Energy https://energy.gov/eere/fuelcells/doe-technical-targets-polymer-electrolyte-membrane-fuel-cell-components, (2017) 30. Doi: https://doi.org/10.2172/1220127.
[57] H. Schulenburg, J. Durst, E. Müller, A. Wokaun, G.G. Scherer, Real surface area measurements of Pt3Co/C catalysts, J. Electroanal. Chem. 642 (2010) 52–60, https://doi.org/10.1016/j.jelechem.2010.02.005.
[58] D.F. Van Der Vliet, C. Wang, D. Li, A.P. Paulikas, J. Greeley, R.B. Rankin, D. Strmcnik, D. Tripkovic, N.M. Markovic, V.R. Stamenkovic, Unique electrochemical adsorption properties of Pt-skin surfaces, Angew. Chemie - Int. Ed. 51 (2012) 3139–3142, https://doi.org/10.1002/anie.201107668.
[59] T.R. Garrick, T.E. Moylan, M.K. Carpenter, A. Kongkanand, Editors' choice—electrochemically active surface area measurement of aged Pt alloy catalysts in PEM fuel cells by CO stripping, J. Electrochem. Soc. 164 (2017) F55–F59, https://doi.org/10.1149/2.0381702jes.
[60] P.A. Heizmann, H. Nguyen, M. von Holst, A. Fischbach, M. Kostelec, F.J. Gonzalez Lopez, M. Bele, L. Pavko, T. Đukić, M. Šala, F. Ruiz-Zepeda, C. Klose, M. Gatalo, N. Hodnik, S. Vierrath, M. Breitwieser, Alternative and facile production pathway towards obtaining high surface area PtCo/C intermetallic catalysts for improved PEM fuel cell performance, RSC Adv. 13 (2023) 4601–4611, https://doi.org/10.1039/d2ra07780a.
[61] J.A. Gilbert, A.J. Kropf, N.N. Kariuki, S. DeCrane, X. Wang, S. Rasouli, K. Yu, P. J. Ferreira, D. Morgan, D.J. Myers, In-operando anomalous small-angle X-ray scattering investigation of Pt 3 co catalyst degradation in aqueous and fuel cell environments, J. Electrochem. Soc. 162 (2015) F1487–F1497, https://doi.org/10.1149/2.0531514jes.
[62] F. Hasché, M. Oezaslan, P. Strasser, Activity, structure and degradation of Dealloyed PtNi 3 nanoparticle Electrocatalyst for the oxygen reduction reaction in PEMFC, J. Electrochem. Soc. 159 (2011) B24–B33, https://doi.org/10.1149/2.030201jes.
[63] Supplier Specifications: 40% Wt Platinum Cobalt (3,1 Atomic Ratio) on Vulcan, (n.d.). https://www.fuelcellstore.com/40-platinum-cobalt-vulcan-3-1-ratio (accessed November 4, 2025).
[64] D.J. Yarusso, S.L. Cooper, Microstructure of ionomers: interpretation of small-angle X-ray scattering data, Macromolecules 16 (1983) 1871–1880, https://doi.org/10.1021/ma00246a013.
[65] X. Jin, J. Yan, X. Liu, Q. Zhang, Y. Huang, Y. Wang, C. Wang, Y. Wu, Spatial confinement of Pt nanoparticles in carbon nanotubes for efficient and selective H2 evolution from methanol, Adv. Sci. 11 (2024) 1–10, https://doi.org/10.1002/advs.202306893.
[66] A.Y. Kurenkova, A.A. Saraev, D.D. Mishchenko, E.Y. Gerasimov, E.A. Kozlova, Influence of Pt oxidation state on the activity and selectivity of g-C3N4-based Photocatalysts in H2 evolution reaction, Appl. Sci. 13 (2023) 11739, https://doi.org/10.3390/app132111739.
[67] S. Takao, O. Sekizawa, K. Higashi, G. Samjeské, T. Kaneko, T. Sakata, T. Yamamoto, T. Uruga, Y. Iwasawa, Visualization analysis of Pt and co species in degraded Pt3Co/C Electrocatalyst layers of a polymer electrolyte fuel cell using a same-view Nano-XAFS/STEM-EDS combination technique, ACS Appl. Mater. Interfaces 12 (2020) 2299–2312, https://doi.org/10.1021/acsami.9b16393.
[68] G. Gebel, O. Diat, Neutron and X-ray scattering: suitable tools for studying lonomer membranes, Fuel Cells 5 (2005) 261–276, https://doi.org/10.1002/fuce.200400080.
[69] G. Gebel, Structural evolution of water swollen perfluorosulfonated ionomers from dry membrane to solution, Polymer (Guildf) 41 (2000) 5829–5838, https://doi.org/10.1016/S0032-3861(99)00770-3.
[70] F. Van Der Linden, E. Pahon, S. Morando, D. Bouquain, A review on the proton-exchange membrane fuel cell break-in physical principles, activation procedures, and characterization methods, J. Power Sources 575 (2023) 233168, https://doi.org/10.1016/j.jpowsour.2023.233168.
[71] F. Maillard, L. Dubau, J. Durst, M. Chatenet, J. André, E. Rossinot, Durability of Pt3Co/C nanoparticles in a proton-exchange membrane fuel cell: direct evidence of bulk co segregation to the surface, Electrochem. Commun. 12 (2010) 1161–1164, https://doi.org/10.1016/j.elecom.2010.06.007.
[72] H. Matsui, N. Ishiguro, T. Uruga, O. Sekizawa, K. Higashi, N. Maejima, M. Tada, Operando 3D visualization of migration and degradation of a platinum cathode catalyst in a polymer electrolyte fuel cell, Angew. Chemie 129 (2017) 9499–9503, https://doi.org/10.1002/ange.201703940.